buildings

MDPI

Article

Economic and Low-Carbon Cementitious Materials Based on Hot–Stuffy Steel Slag

Xupeng Zhang [1], Changze Xu [2,3], Mingze Wang [4], Shirong Du [4], Yan Li [1,5,*] and Guoqing Wang [4,5,*]

[1] School of Civil Engineering and Architecture, Hainan University, Haikou 570228, China; 20223001146@hainanu.edu.cn
[2] School of Civil Engineering, Southwest Jiaotong University, Chengdu 610031, China; sjyqlsjy@163.com
[3] Shandong Provincial Communications Planning and Design Institute Group Co., Ltd., Jinan 250101, China
[4] School of Materials Science and Engineering, Hainan University, Haikou 570228, China; 23210805000005@hainanu.edu.cn (M.W.); 24210805000001@hainanu.edu.cn (S.D.)
[5] State Key Laboratory of Tropic Ocean Engineering Materials and Materials Evaluation, Hainan University, Haikou 570228, China
* Correspondence: 990455@hainanu.edu.cn (Y.L.); wangguoqing@hainanu.edu.cn (G.W.)

Abstract

Ordinary steel slag serves as a supplementary cementitious material (SCMs) to enhance the resource efficiency of industrial waste and contribute to decarbonization and economic benefits. However, there are significant differences in the composition and properties between hot–stuffy steel slag and ordinary steel slag, and there has been little research focusing on hot–stuffy steel slag as an SCM. Herein, we investigated the application of hot–stuffy steel slag, coal bottom ash, slag powder, desulfurization gypsum, and cement as raw materials for developing new green, low-carbon, and economical cementitious materials. When the hot–stuffy steel slag content was 20%, the compressive and flexural strengths of the cementitious material at 28 days reached as high as 64.5 MPa and 11.3 MPa, respectively. Even when the hot–stuffy steel slag content is increased to 50%, the compressive and flexural strengths at 28 days remain 58.2 MPa and 6.1 MPa, respectively. Furthermore, an X-ray diffractometer (XRD) and scanning electron microscopy (SEM) show that the hydration products generated by the new low-carbon cementitious materials (LCM) are mainly C-(A)-S-H gels. Mercury intrusion porosimetry (MIP) indicates that when the hot–stuffy steel slag content is 20%, the total porosity (18.85%) of the LCM is the lowest, suggesting that the lower the porosity, the better the strength. Notably, the heavy metal ions released by hot–stuffy steel slag-based cementitious materials were far below hygienic standards for drinking water, confirming their ability to fix heavy metal ions. This work provides an excellent model and application prospect for the utilization of hot–stuffy steel slag in non-structural engineering projects such as river engineering, marine engineering, and road engineering, enabling the achievement of both low-carbon and economic objectives.

Keywords: hot–stuffy steel slag; slag powder; coal bottom ash; desulfurized gypsum; cementitious material

check for updates

Academic Editor: Eugeniusz Koda

Received: 19 July 2025
Revised: 9 August 2025
Accepted: 16 August 2025
Published: 19 August 2025

Citation: Zhang, X.; Xu, C.; Wang, M.; Du, S.; Li, Y.; Wang, G. Economic and Low-Carbon Cementitious Materials Based on Hot–Stuffy Steel Slag. *Buildings* **2025**, *15*, 2931. https://doi.org/10.3390/buildings15162931

Copyright: © 2025 by the authors. Licensee MDPI, Basel, Switzerland. This article is an open access article distributed under the terms and conditions of the Creative Commons Attribution (CC BY) license (https://creativecommons.org/licenses/by/4.0/).

1. Introduction

The cement industry accounts for about 8% of the total CO_2 emissions, which have a severe impact on global climate change and exacerbate global warming [1–3]. To reduce CO_2 emissions, industrial solid waste can be used as LCM to partially replace cement, thereby reducing cement consumption. Steel manufacturing is an indispensable industry

in the development process of all countries [4]. Steel slag is a solid waste product generated during steel manufacturing [1,5,6], accounting for approximately 10% to 15% of the steel output [1,7,8]. A large amount of steel slag generated will face high disposal costs [7]; therefore, the recycling of steel slag offers economic benefits. In China, steel slag production exceeded 180 million tons in 2023 and 93 million tons in 2013 [6]; its production is increasing year by year, but its comprehensive utilization rate remains extremely low [9–11], leading to issues such as land occupation [12–15], resource waste [16], environmental pollution [13–17], low economic benefits [17], and heavy metal pollution [18,19]. Coal bottom ash is the solid residue deposited at the bottom of high-temperature furnaces from power plants [20,21]. Slag powder is a solid waste product from the steel production process [22,23], with its production typically accounting for 5% to 10% of steel production. Desulfurization gypsum is a byproduct generated during the desulfurization of sintering flue gases in steel plants [24–26]. The recycling and utilization of solid waste has become a global urgent task for protecting the ecological environment and promoting sustainable development [15].

Studies have indicated that steel slag and slag powder possess certain similarities with cement clinker in terms of their mineral compositions [27–29]. Studies have shown that steel slag can be used as a substitute for aggregates in building materials [10]. Additionally, numerous researchers have conducted investigations related to the application of SCMs [30–33], including steel slag [32–35], slag powder [36], fly ash [34,37–39], silica fume [31,33,38,40], red mud [32,35,41,42], and metakaolin [36,39,43]. Hot–stuffy steel slag is special steel slag that has undergone hot stuffy self-disintegration treatment [44]. It has a mineral composition that includes dicalcium silicate (C_2S) and tricalcium silicate (C_3S) [27], providing the basis for cementitious activity. During the production of hot–stuffy steel slag, f-MgO and f-CaO react with water due to the hot stuffy self-disintegration, leading to a decrease in their content and improved volume stability [45,46]. In previous studies, hot–stuffy steel slag was used in epoxy coatings [47], unburned ceramsites [48], thermal conductive asphalt concretes for snow melting pavements [49], etc. However, research on hot–stuffy steel slag as an SCM is limited and insufficient. In this study, a new type of LCM was prepared by combining hot–stuffy steel slag, coal bottom ash, slag powder, cement, and desulfurization gypsum. The effect of steel slag content on the setting time, microstructure, compressive strength, and flexural strength was investigated. Moreover, the cementitious materials were characterized using X-ray diffraction, scanning electron microscopy, energy dispersive spectroscopy, and an inductively coupled plasma optical emission spectrometer. When the hot–stuffy steel slag content was 20%, the compressive and flexural strengths of the cementitious material at 28 days reached as high as 64.5 MPa and 11.3 MPa, respectively. Additionally, the toxic heavy metals released by cementitious materials are far below the standards for toxic metal ions in drinking water, indicating their ability to effectively immobilize heavy metals. This work provides a sustainable and green path for high-content hot–stuffy steel slag to be utilized in the river engineering, marine engineering, and road engineering fields.

2. Materials and Methods

2.1. Raw Material

The hot–stuffy steel slag, coal bottom ash, slag powder, and desulfurization gypsum used in this experiment were all sourced from Baowu Huanke (Resource Recycling Co., Ltd., Zhanjiang, China). The ordinary Portland cement (PO 52.5) used in the experiment was derived from commercial cement (Jiuqi Building Materials Co., Ltd, Zhucheng, China).

The composition and the specific surface area of hot–stuffy steel slag, coal bottom ash, slag powder, and desulfurization gypsum are shown in Table 1. The Dandong Bettersize

BT-9300LD laser particle size meter is used to test the specific surface area according to GB/T 19077-2016 [50].

Table 1. Chemical composition (wt.%) and specific surface area (m^2/kg) of the raw materials. (The tested heavy metal includes Cr, Co, Ni, Cu, Zn, Mo, and Ba.)

Composition	SiO_2	Al_2O_3	CaO	MgO	Fe_2O_3	SO_3	P_2O_5	Heavy Metal	SSA
Hot–stuffy steel slag	9.64	7.57	44.23	4.50	26.72	0.34	1.53	0.58	297.6
Coal bottom ash	55.68	23.69	5.79	0.69	8.47	0.18	0.14	0.18	281.1
Slag powder	27.95	13.87	45.84	6.67	0.54	2.65	0.01	0.43	227.0
Desulfurization gypsum	1.18	0.49	49.56	0.10	0.24	46.24	0.01	-	224.3
Cement	23.89	8.23	54.83	4.42	3.73	3.10	0.13	-	-

The particle size distribution and XRD are presented in Figure 1, and the SEM images are shown in Figure 2. The particle size of hot–stuffy steel slag ranged from 1.030 to 168.1 μm, with a medium particle size ($D_{[50]}$) of 36.90 μm, an average volume diameter ($D_{[4,3]}$) of 49.95 μm, and a specific surface area of 297.6 m^2/kg. The main mineral phases of hot–stuffy steel slag include dicalcium silicate (C_2S) and tricalcium silicate (C_3S) [47,51]. The particle size of the coal bottom ash ranged from 1.035 to 171.3 μm, with a medium particle size ($D_{[50]}$) of 45.07 μm, an average volume diameter ($D_{[4,3]}$) of 55.22 μm, and a specific surface area of 281.1 m^2/kg. The X-ray diffraction pattern of the coal bottom ash showed a significant peak at 2θ = 20.9°, 26.6°, 29.8°, and 36.5°, verifying the presentence of the SiO_2 [52,53]. The particle size of the slag powder ranged from 1.585 to 133.2 μm, with a medium particle size ($D_{[50]}$) of 28.90 μm, an average volume diameter ($D_{[4,3]}$) of 40.11 μm, and a specific surface area of 227.0 m^2/kg. The X-ray diffraction spectrum of the slag powder showed typical amorphous structure characteristics [54]. The particle size of the desulfurization gypsum ranged from 2.344 to 62.67 μm, with a medium particle size ($D_{[50]}$) of 16.80 μm, an average volume diameter ($D_{[4,3]}$) of 21.18 μm, and a specific surface area of 224.3 m^2/kg. The corresponding characteristic peaks in XRD indicate that desulfurization gypsum mainly consists of calcium sulfate [25].

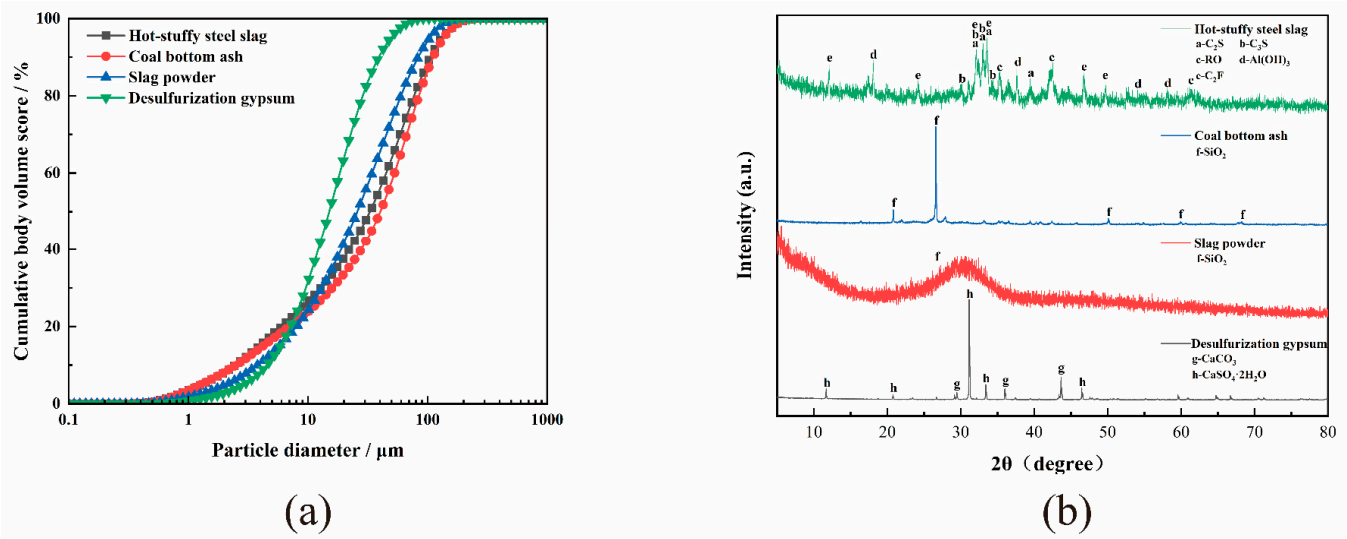


Figure 1. (**a**) Particle size of the raw materials; (**b**) XRD patterns of the raw materials.

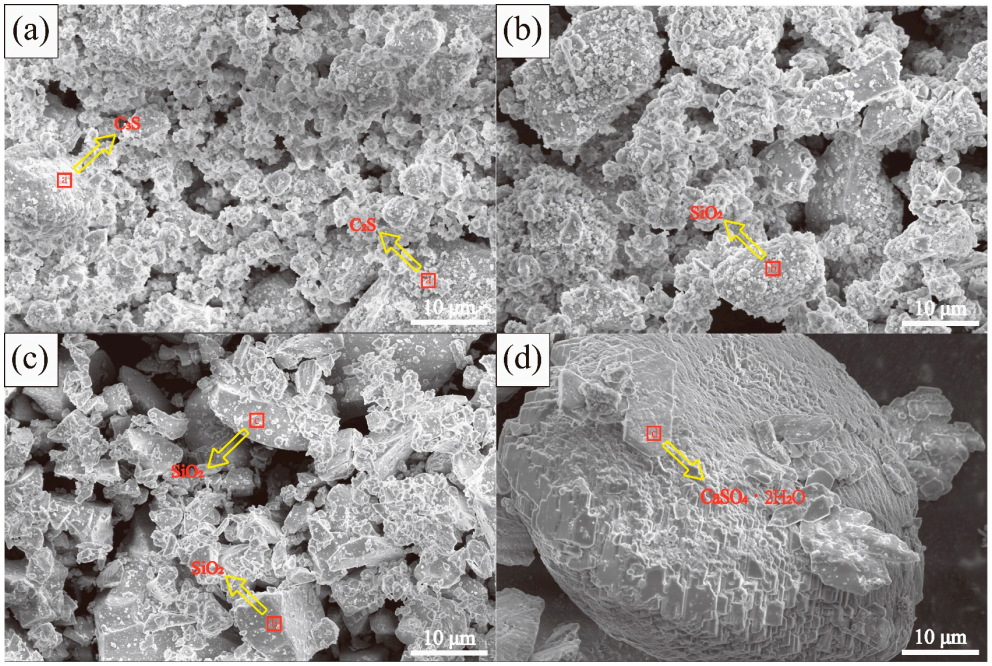


Figure 2. SEM images of the raw materials: (**a**) hot–stuffy steel slag; (**b**) coal bottom ash; (**c**) slag powder; and (**d**) desulfurization gypsum.

2.2. Preparation of Cementitious Materials

Table 2 provides the mixing ratios of hot–stuffy steel slag, ordinary Portland cement (PO 52.5), slag powder, coal bottom ash, and desulfurization gypsum in the cementitious materials.

Table 2. Mixing ratios of hot–stuffy steel slag, ordinary Portland cement (PO 52.5), slag powder, coal bottom ash, and desulfurization gypsum in the cementitious materials. (wt.%).

Sample No.	Hot–Stuffy Steel Slag	Cement	Slag Powder	Coal Bottom Ash	Desulfurization Gypsum
1	10	28	42	10	10
2	20	24	36	10	10
3	30	20	30	10	10
4	40	16	24	10	10
5	50	12	18	10	10

The raw materials were mixed using a planetary mixer. Then, water was added and stirred for 150 s. After that, cement paste was poured into prismatic specimens with dimensions of 40 mm × 40 mm × 120 mm and 40 mm × 40 mm × 40 mm, followed by 3 min of vibration. The water-to-solid ratio was 0.3. The specimens were placed in a curing room at (20 ± 2) °C and a relative humidity > 95%.

2.3. Experimental Procedure

Figure 3 shows the experimental procedure of economic and low-carbon cementitious materials based on hot–stuffy steel slag. The setting times are determined according to standard GB/T1346-2011 [55]. According to the GB/T 17671-1999 [56], compression strength tests are conducted on a universal testing machine at a loading rate of 2.4 kN/s, with specimen dimensions of 40 mm × 40 mm × 40 mm. Based to the GB/T 17671-1999 standard, flexural strength tests are conducted on specimens with dimensions of 40 mm × 40 mm × 120 mm using a three-point bending device on a universal testing machine with a loading rate of 50.0 N/s. The XRD pattern was obtained by an X-ray diffractometer (Smart Lab SE, Rigaku, Japan). SEM and EDS images were captured by a

scanning electron microscope (Quattro S, Thermo Fisher, Czech). The Agilent ICP-MS 7800 (Agilent Technologies Inc., Japan) was employed to assess the concentration of toxic metal ions released from cementitious materials. The pore structure of the LCM was obtained using the Auto Pore IV 9520 instrument (Micromeritics Instruments, Micromeritics Instrument Co. Ltd, USA).

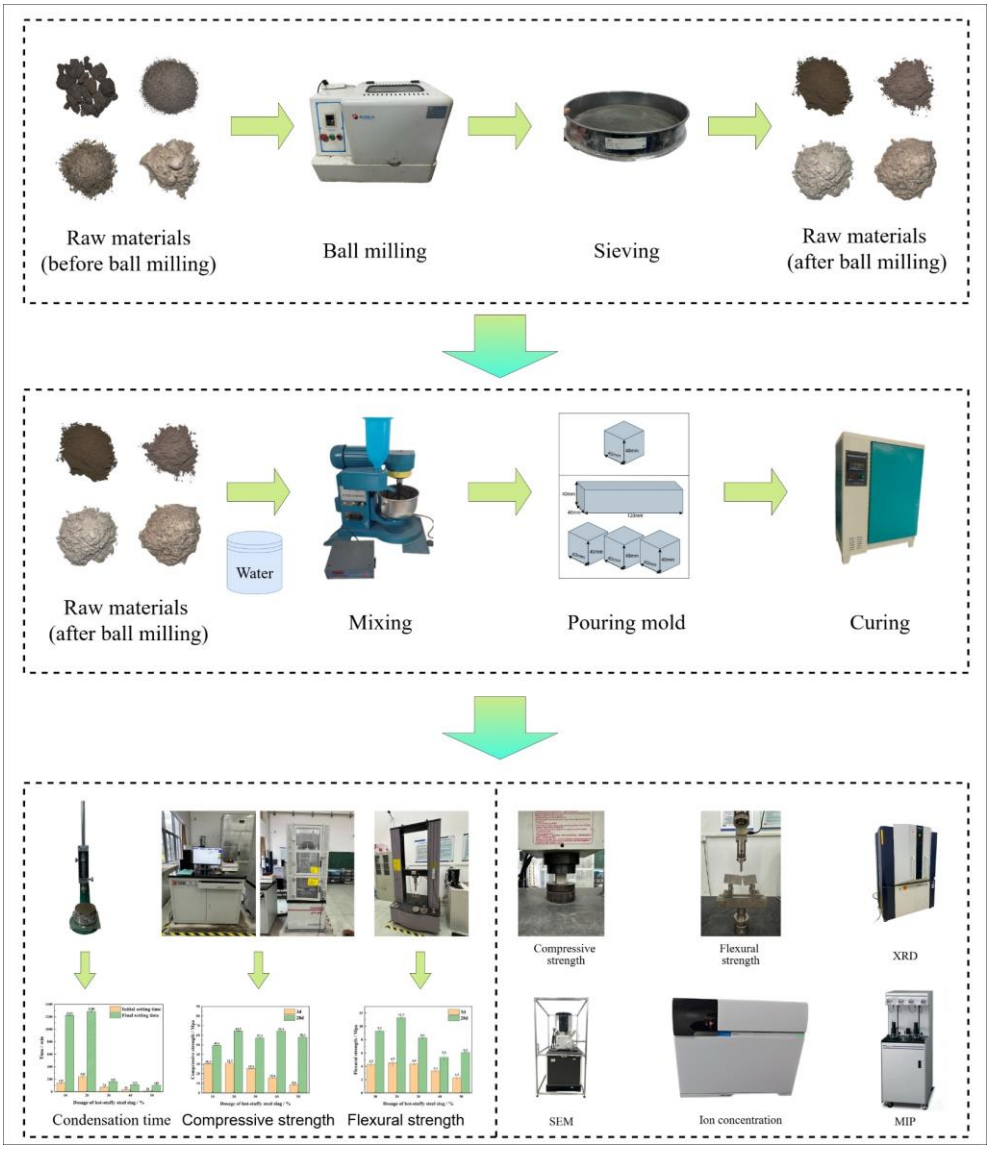


Figure 3. Experimental procedure.

3. Results and Discussions

3.1. Setting Times

Figure 4 shows the setting time of the LCM with different concentrations of hot–stuffy steel slag. When the hot–stuffy steel slag content is 10%, 20%, 30%, 40%, and 50%, respectively, the initial setting times of the cementitious materials are 141 min, 242 min, 74 min, 34 min, and 16 min, respectively, and the final setting times are 1223 min, 1288 min, 163 min, 114 min, and 105 min, respectively. As the proportion of hot–stuffy steel slag increases, the initial and final setting times of the cementitious materials exhibit a trend of first prolonging and then shortening. When the proportion of hot-stuffy steel slag is 50%, the initial and final setting times are shortened by 226 min and 1183 min, respectively, compared to those with a 20% proportion of hot–stuffy steel slag.

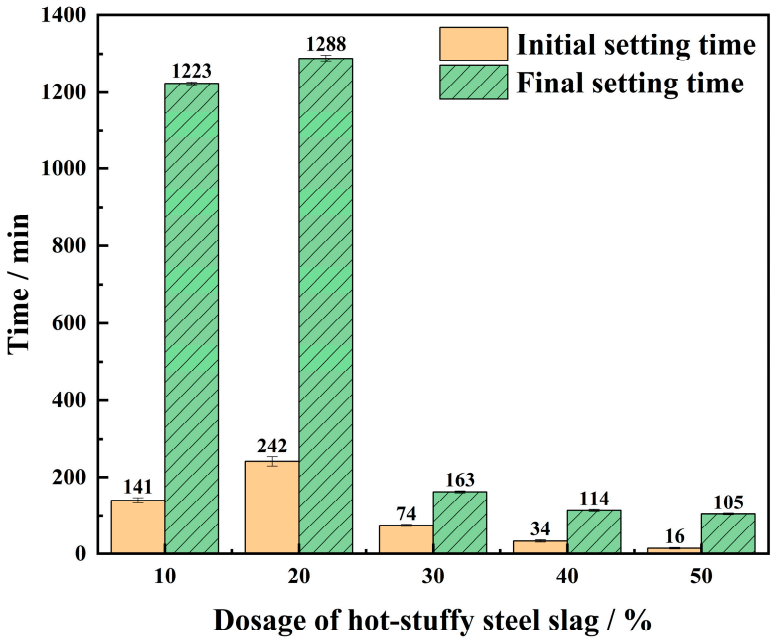


Figure 4. Initial and final setting times of the cementitious materials with different dosages of hot–stuffy steel slag.

3.2. Compressive Strength and Flexural Strength

Figure 5 shows the compressive and flexural strengths of the new LCM with different dosages of hot–stuffy steel slag. As shown in Figure 5a, the compressive strength of the cementitious material exhibits a trend of first increasing and then decreasing as the dosage of hot–stuffy steel slag gradually increases. When the dosage of hot–stuffy steel slag is 10%, 20%, 30%, 40%, and 50%, the corresponding 3-day compressive strengths for each group are 30.4 MPa, 31.3 MPa, 25.4 MPa, 15.6 MPa, and 8.6 MPa, respectively, while the 28-day compressive strengths were 49.4 MPa, 64.5 MPa, 57.3 MPa, 64.4 MPa, and 58.2 MPa, respectively. As shown in Figure 5b, with the gradual increase in the amount of hot–stuffy steel slag, the flexural strength of the cementitious material system initially rises and then drops. When the amounts of hot–stuffy steel slag are 10%, 20%, 30%, 40%, and 50%, respectively, the 3-day flexural strengths are 4.3 MPa, 4.5 MPa, 4.4 MPa, 3.3 MPa, and 2.3 MPa, respectively, while the 28-day flexural strengths were 9.3 MPa, 11.3 MPa, 8.3 MPa, 5.4 MPa, and 6.1 MPa, respectively. It is worth noting that when the steel slag content is 20%, its compressive and flexural strengths can reach as high as 64.5 MPa and 11.3 MPa, respectively. Therefore, this novel, economical, and low-carbon cementitious material based on solid waste can be widely used in non-structural engineering and precast components.

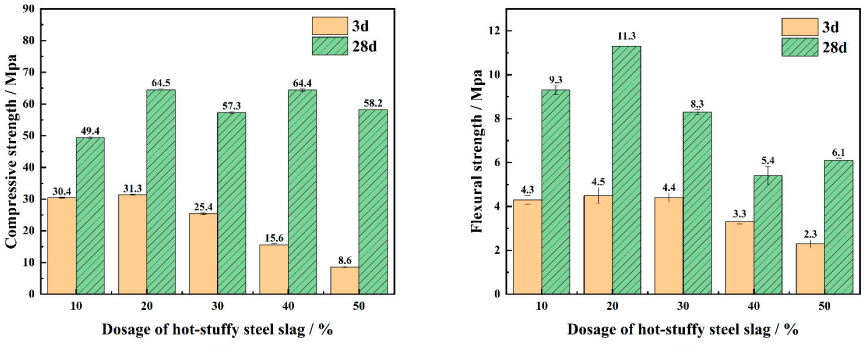


Figure 5. (**a**) Compressive strength and (**b**) flexural strength of the cementitious materials with different dosages of hot–stuffy steel slag.

3.3. Ion Concentration Measurement

Table 3 and Figure 6 show the concentrations of toxic heavy metal ions leached from the cementitious materials. The concentrations of Cd, Cr, Mn, and Pb were 0.0006 mg/L, 0.0471 mg/L, 0.0017 mg/L, and 0.0006 mg/L, respectively, which are far below the concentration requirements for heavy metal elements specified in the "Drinking Water Hygiene Standards" (GB5749-2022 [57]) and the "Comprehensive Wastewater Discharge Standards" (GB 8978-1996 [58]). This indicates that the cementitious material has a dense structure that can suppress the leaching of heavy metal elements from the raw materials, making it suitable not only for the encapsulation of toxic metal tailings but also for river engineering and marine engineering applications.

Table 3. Cumulative release of Cd, Cr, Mn, and Pb from the cementitious materials with water curing conditions (mg/L).

Heavy Metal Elements	Concentration	Hygienic Standards for Drinking Water	Comprehensive Sewage Discharge Standards
Cd	0.0006	≤0.005	≤0.1
Cr	0.0471	≤0.05	≤1.5
Mn	0.0017	≤0.1	≤2.0
Pb	0.0006	≤0.01	≤1.0

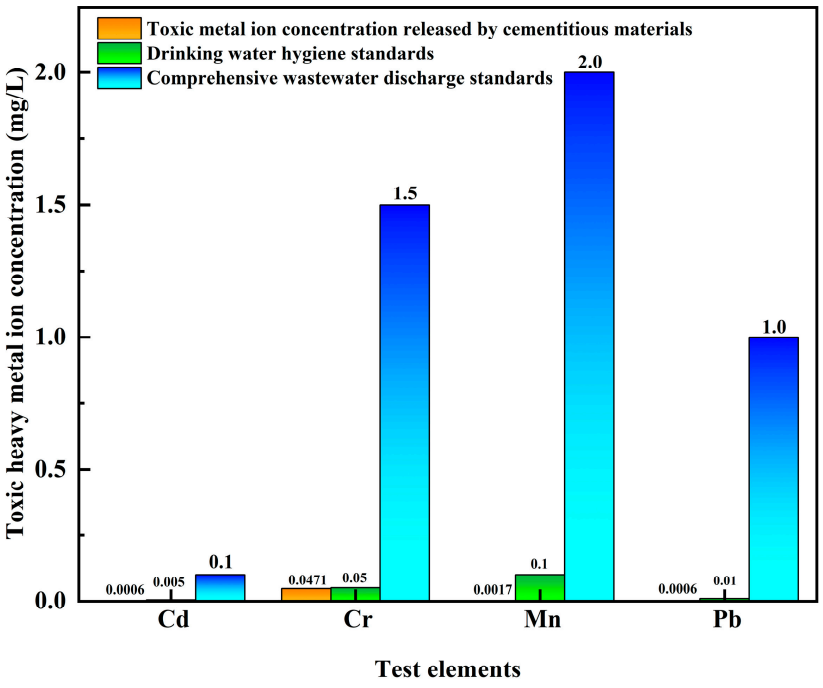


Figure 6. Cumulative release of Cd, Cr, Mn, and Pb from the cementitious materials (mg/L).

3.4. MIP

Figure 7 shows the cumulative pore volume, the pore size distributions, and the proportion of different pore sizes of the cementitious materials with different dosage of hot–stuffy steel slag. The cumulative pore volume curve (Figure 7a) indicates that the cementitious material with 20% steel slag content has the smallest cumulative pore volume, while the cementitious material with 50% steel slag content has the largest cumulative pore volume. When the steel slag content is 10, 20, 30, 40, and 50%, the peak pore sizes of the cementitious material are 21.6, 21.6, 25.6, 30.4, and 25.6 nm, respectively (Figure 7b). When the hot–stuffy steel slag content is 10%, 20%, 30%, 40%, and 50%, respectively, the pores

of cementitious material with diameters greater than 1000 nm (red) account for 10%, 15%, 11%, 12%, and 12%, respectively (Figure 7c). Pores with diameters greater than 100 nm but less than 1000 nm (blue) account for 6%, 8%, 5%, 6%, and 4%, respectively. Pores with diameters greater than 10 nm but less than 100 nm (orange) account for 68%, 56%, 66%, 65%, and 69%, respectively. Pores with diameters less than 10 nm (green) account for 16%, 21%, 18%, 17%, and 15%, respectively. When the hot–stuffy steel slag content is 20%, the total porosity (18.85%) of the cementitious material is the lowest, with the pores primarily consisting of small- and medium-sized pores (Figure 7c), indicating that the cementitious material is denser, thereby achieving higher strength.

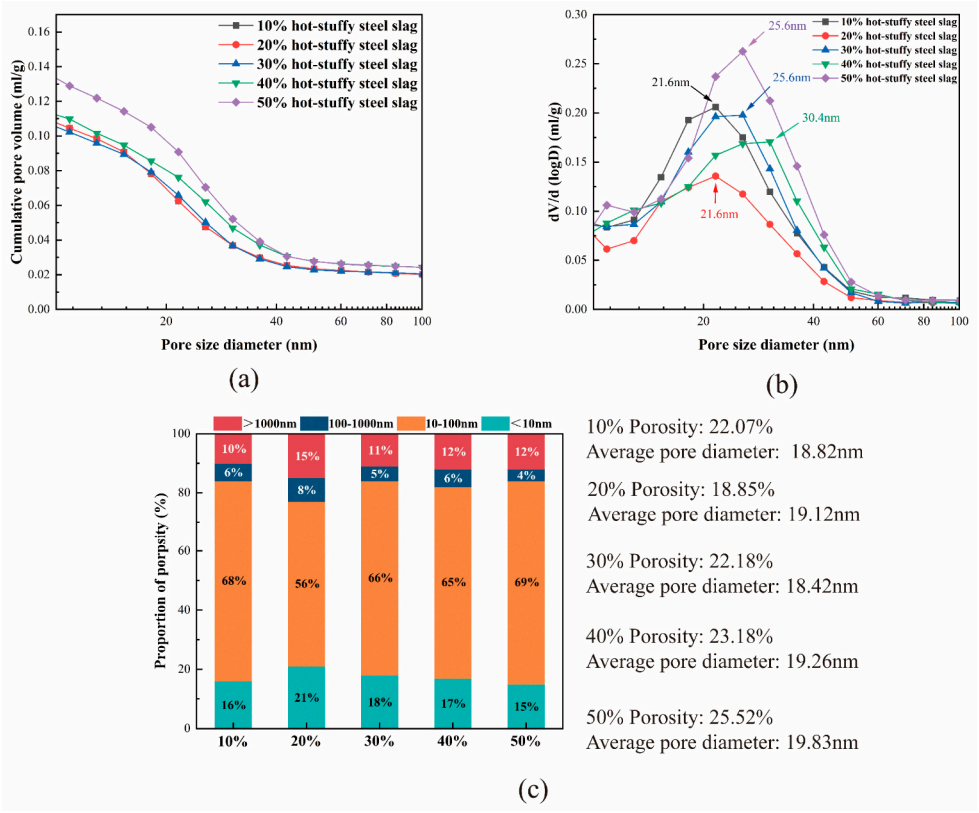


Figure 7. (**a**) The cumulative pore volume, (**b**) the pore size distributions, and (**c**) the proportion of different pore sizes of the cementitious materials with different dosages of hot–stuffy steel slag.

3.5. SEM and EDS Analysis

Figure 8 shows the SEM images, EDS mapping, and spectrum of cementitious materials with different hot–stuffy steel slag contents after 3 days and 28 days of curing. The EDS mapping and spectrum indicate that the primary elements present in the LCM include C, O, Mg, Al, Si, S, Ca, Fe, K, etc. As shown in the SEM images, the products generated by the C-(A)-S-H gel reaction are flocculent, uniformly distributed, and mutually bonded particles that form a strong skeleton, which provides the corresponding strength for the LCM. Desulfurization gypsum provides SO_4^{2-}, and hot–stuffy steel slag provides active Al_2O_3, which together form calcium aluminate (AFt) with needle-like/columnar crystals. These crystals fill microscopic pores and inhibit crack propagation, making the LCM denser and significantly enhancing early strength and structural toughness.

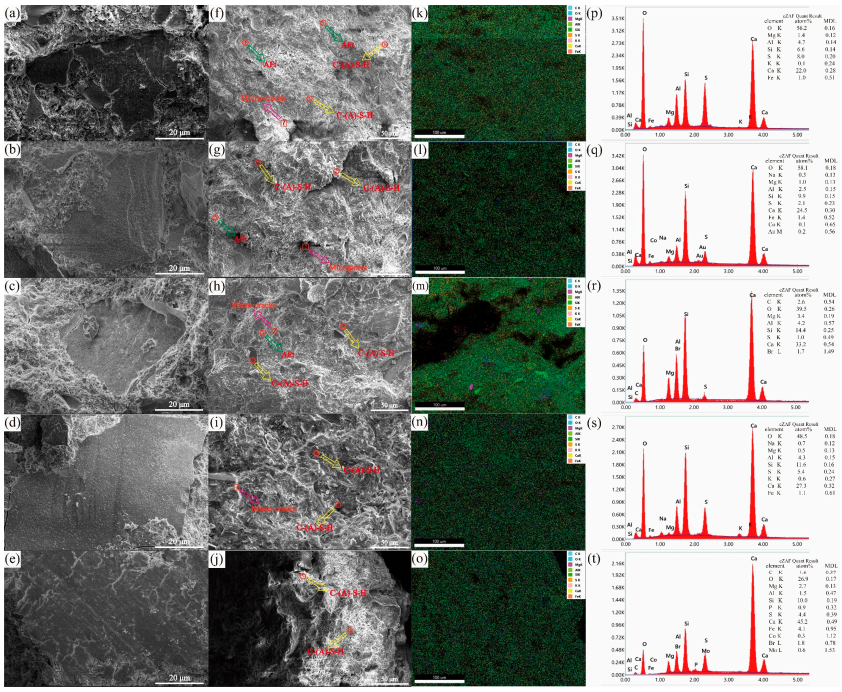
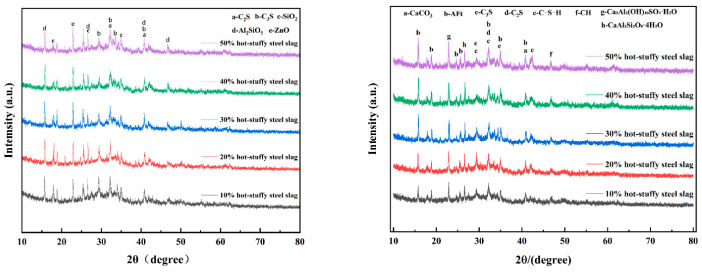


Figure 8. SEM images of 3d cementitious materials with (**a**) 10%, (**b**) 20%, (**c**) 30%, (**d**) 40%, and (**e**) 50% dosages of hot–stuffy steel slag. SEM images of 28d cementitious materials with (**f**) 10%, (**g**) 20%, (**h**) 30%, (**i**) 40%, and (**j**) 50% dosages of hot–stuffy steel slag. EDS mapping and spectrum of 28d cementitious materials with (**k**,**p**) 10%, (**l**,**q**) 20%, (**m**,**r**) 30%, (**n**,**s**) 40%, and (**o**,**t**) 50% dosages of hot–stuffy steel slag.

3.6. XRD Analysis

Figure 9 shows the XRD results of cementitious materials with different hot–stuffy steel slag contents after 3 days and 28 days of curing. The hydration products of cementitious materials with different hot–stuffy steel slag contents are basically the same after 3 days of curing, mainly including C_2S, C_3S, SiO_2, Al_2SiO_5, ZnO, etc. The C_2S and C_3S phases provide the main strength support for the cementitious materials. After 28 days of curing, the hydration products of the LCM mainly include $CaCO_3$, AFt, C_3S, C_2S, C-S-H, CH, $Ca_3Al_2(OH)_{10}SO_4{\cdot}H_2O$, and $CaAl_2Si_2O_8{\cdot}4H_2O$ (C-A-S-H). The results are consistent with SEM images. C-S-H and C-A-S-H can provide strength for the LCM. The C-S-H, C-A-S-H, and AFt can fill micropores and inhibit the formation of microcracks. Notably, the porosity of LCMs decreases, and their strength is enhanced.



(a) (b)

Figure 9. XRD Analysis of (**a**) 3d and (**b**) 28d cementitious materials with different dosages of hot–stuffy steel slag.

4. Conclusions

In this study, we utilized hot–stuffy steel slag to prepare a novel LCM and investigated the effects of hot–stuffy steel slag content on the initial and final setting times, as well

as the compressive and flexural strengths of the cementitious materials. Additionally, we characterized the raw materials, including hot-stuffy steel slag, coal bottom ash, slag powder and desulfurization gypsum, using X-ray diffraction, scanning electron microscopy, energy dispersive spectroscopy, and inductively coupled plasma mass spectrometry. The initial setting time and final setting time of the cementitious material first increase and then decrease with an increase in the amount of hot-stuffy steel slag. When the hot–stuffy steel slag content reaches 20%, the 28-day compressive strength of the cementitious materials reaches as high as 64.5 MPa, and the flexural strength reaches as high as 11.3 MPa. The concentrations of heavy metal elements in the leachate solution of water-cured cementitious material (Cd: 0.0006 mg/L, Cr: 0.0471 mg/L, Mn: 0.0017 mg/L, Pb: 0.0006 mg/L) were far below the limits specified in the "Drinking Water Hygiene Standards" (GB 5749-2022) and the "Comprehensive Wastewater Discharge Standards" (GB 8978-1996). SEM, XRD, and MIP analyses indicate that the high strength of the cementitious material is primarily due to the formation of C-(A)-S-H and AFt, as well as the extremely low porosity. These characteristics make the LCMs denser and give them improved integrity. The new LCM exhibits excellent mechanical properties, heavy metal retention capabilities, and the ability to recycle various industrial solid wastes, which can be widely used in river engineering, marine engineering, building materials engineering, and road engineering. This work achieves the resource utilization of industrial solid wastes such as hot–stuffy steel slag, coal bottom ash, slag powder, and desulfurization gypsum, reduces the consumption of cement clinker, and provides a feasible pathway for the application of high-value solid wastes.

Author Contributions: Conceptualization, X.Z., Y.L. and G.W.; methodology, X.Z.; validation, X.Z., Y.L. and X.Z.; formal analysis, X.Z., C.X. and M.W.; investigation, X.Z., M.W. and S.D.; data curation, X.Z., M.W. and S.D.; writing—original draft preparation, X.Z.; writing—review and editing, X.Z.; visualization, X.Z.; supervision, X.Z., Y.L. and G.W.; project administration, X.Z., Y.L. and G.W.; funding acquisition, Y.L. All authors have read and agreed to the published version of the manuscript.

Funding: This research was funded by the Program of Education and Teaching Reform in Hainan University, (No. Hnjg2025-9).

Data Availability Statement: The data are available on request.

Acknowledgments: The author would like to thank the Analysis and Testing Center of Hainan University.

Conflicts of Interest: Author Changze Xu was employed by the company Shandong Provincial Communications Planning and Design Institute Group Co., Ltd. The remaining authors declare that the research was conducted in the absence of any commercial or financial relationships that could be construed as a potential conflict of interest.

References

1. Gencel, O.; Karadag, O.; Oren, O.H.; Bilir, T. Steel slag and its applications in cement and concrete technology: A review. *Constr. Build. Mater.* **2021**, *283*, 122783. [CrossRef]
2. Cremona, R.; De Lena, E.; Conversano, A.; Spinelli, M.; Romano, M.C.; Gatti, M. Techno-economic assessment of high temperature heat pumps integrated in MEA-based post-combustion CO_2 capture for cement plant. *Carbon Capture Sci. Technol.* **2025**, *16*, 100446. [CrossRef]
3. Song, J.; Wang, X.; Chen, Y.; Mi, R.; Zhang, D.; Li, J.; Mao, Y.; Wang, W. Performance comparison of solid waste-derived sulfoaluminate cement and Portland cement under air curing and CO_2 curing. *Constr. Build. Mater.* **2025**, *482*, 141629. [CrossRef]
4. Naidu, T.S.; Sheridan, C.M.; van Dyk, L.D. Basic oxygen furnace slag: Review of current and potential uses. *Miner. Eng.* **2020**, *149*, 106234. [CrossRef]
5. Cui, P.; Zhou, X.; Xiao, Y.; Wang, F. Enhanced environmental and self-healing performance of asphalt mixture using steel slag as the substrate of functional coatings. *Constr. Build. Mater.* **2025**, *489*, 142427. [CrossRef]
6. Huang, X.; Wang, Z.; Liu, Y.; Hu, W.; Ni, W. On the use of blast furnace slag and steel slag in the preparation of green artificial reef concrete. *Constr. Build. Mater.* **2016**, *112*, 241–246. [CrossRef]

7. Gu, J.; Wei, C.; Wu, P.; Cao, Z.; Shao, Y.; Liu, X.; Zhang, Z. Application and mechanism analysis of steel slag in resource recovery and environmental remediation: A review. *Miner. Eng.* **2025**, *227*, 109268. [CrossRef]
8. Gao, T.; Dai, T.; Shen, L.; Jiang, L. Benefits of using steel slag in cement clinker production for environmental conservation and economic revenue generation. *J. Clean. Prod.* **2021**, *282*, 124538. [CrossRef]
9. Yi, H.; Xu, G.; Cheng, H.; Wang, J.; Wan, Y.; Chen, H. An Overview of Utilization of Steel Slag. *Procedia Environ. Sci.* **2012**, *16*, 791–801. [CrossRef]
10. Guo, J.; Bao, Y.; Wang, M. Steel slag in China: Treatment, recycling, and management. *Waste Manag.* **2018**, *78*, 318–330. [CrossRef] [PubMed]
11. Gan, Y.; Li, C.; Zou, J.; Wang, W.; Yu, T. Evaluation of the impact factors on the leaching risk of steel slag and its asphalt mixture. *Case Stud. Constr. Mater.* **2022**, *16*, e01067. [CrossRef]
12. Sun, J.; Huang, W.; Wang, X.; Hu, J.; Wang, Y.; Zhang, Z.; Luo, S. Feasibility of pretreated steel slag for asphalt pavement application and risk assessment of hazardous substance leaching. *Chem. Eng. J.* **2024**, *498*, 155497. [CrossRef]
13. Zhang, Y.; Zhu, G.; Zhang, Y.; Wu, X.; Zhang, F.; Zhang, J.; Li, X. Hydration behavior and cementitious properties of steel slag: From an early age to a long-term. *Case Stud. Constr. Mater.* **2024**, *20*, e03066. [CrossRef]
14. Fu, S.; Kwon, E.E.; Lee, J. Upcycling steel slag into construction materials. *Constr. Build. Mater.* **2024**, *444*, 137882. [CrossRef]
15. Nunes, V.A.; Borges, P.H.R. Recent advances in the reuse of steel slags and future perspectives as binder and aggregate for alkali-activated materials. *Constr. Build. Mater.* **2021**, *281*, 122605. [CrossRef]
16. Fan, C.; Wei, R.; Cheng, T.; Sun, R.; Zhang, H.; Long, H. The positive contributions of steel slag in reducing carbon dioxide emissions in the steel industry: Waste heat recovery, carbon sequestration, and resource utilization. *Chem. Eng. J.* **2024**, *498*, 155379. [CrossRef]
17. Zhong, T.; Zheng, Y.; Chen, Z.; Yao, L.; Zhang, W.; Zhu, Y.; Fu, L. Utilization of steel slag as coarse aggregate and filler in stone mastic asphalt (SMA) mixture: Engineering performance, environmental impact and economic benefits analysis. *J. Clean. Prod.* **2024**, *450*, 141891. [CrossRef]
18. Ren, J.; Shao, J.; Liu, M.; Zhu, H.; Li, M.; Ma, R.; Liang, L.; Mao, J.; Wang, D. The improvement on the properties and heavy metal solidification of phosphogypsum-steel slag cementitious material: Enhancement from Bi-directional carbonation. *Constr. Build. Mater.* **2024**, *457*, 139435. [CrossRef]
19. Zhang, Q.; Yu, X.; Yang, Y.; Ruan, J.; Zou, Y.; Wu, S.; Chen, F.; Zhu, R. Enhanced ammonia removal in tidal flow constructed wetland by incorporating steel slag: Performance, microbial community, and heavy metal release. *Sci. Total Environ.* **2024**, *922*, 171333. [CrossRef]
20. Chen, B.; Ye, G. Enhancing the reaction of municipal solid waste incineration (MSWI) bottom ash in blast furnace slag-based alkali-activated blends: A novel strategy and underlying mechanism. *Cem. Concr. Compos.* **2025**, *160*, 106056. [CrossRef]
21. Zhou, X.; Shen, J. Micromorphology and microstructure of coal fly ash and furnace bottom slag based light-weight geopolymer. *Constr. Build. Mater.* **2020**, *242*, 118168. [CrossRef]
22. Teng, S.; Lim, T.Y.D.; Sabet Divsholi, B. Durability and mechanical properties of high strength concrete incorporating ultra fine Ground Granulated Blast-furnace Slag. *Constr. Build. Mater.* **2013**, *40*, 875–881. [CrossRef]
23. Li, M.; Zhao, H.; Hao, B.; Gao, S.; Liu, R.; Zhu, Z.; Liu, P.; Wang, C.; Shen, P. Study on the mechanical properties and failure behavior of slag cement under dynamic and static loads. *Mater. Today Commun.* **2025**, *47*, 113189. [CrossRef]
24. Dong, L.; Jiao, F.; Liu, W.; Zhang, Z. A new technology for solidification and separation of calcium fluoride from overhaul slag: Synergistic desulfurization gypsum roasting and flotation. *J. Environ. Chem. Eng.* **2025**, *13*, 117881. [CrossRef]
25. Liu, Y.; Wang, Y.; Yin, T.; Lin, C.; Tan, H.; Hariana, H. CO_2 mineralization characteristics of Ca^{2+}-rich leachate from desulfurization gypsum and the regulation of $CaCO_3$ crystal and morphology. *J. Cryst. Growth* **2025**, *667*, 128273. [CrossRef]
26. Koralegedara, N.H.; Pinto, P.X.; Dionysiou, D.D.; Al-Abed, S.R. Recent advances in flue gas desulfurization gypsum processes and applications—A review. *J. Environ. Manag.* **2019**, *251*, 109572. [CrossRef]
27. Ryu, G.U.; Kim, H.J.; Yu, H.J.; Pyo, S. Utilization of steelmaking slag in cement clinker production: A review. *J. CO2 Util.* **2024**, *84*, 102842. [CrossRef]
28. Dai, S.; Zhu, H.; Zhang, D.; Liu, Z.; Cheng, S.; Zhao, J. Insights to compressive strength, impermeability and microstructure of micro-expansion steel slag cement under constraint conditions. *Constr. Build. Mater.* **2022**, *326*, 126540. [CrossRef]
29. Zhao, D.; Zhang, D.; Shen, W.; Huang, J.; Tang, X.; Yang, Y.; Deng, Y.; Wang, Y. Investigation on industrial trial production of multi-phased clinker with crude granular steel slag. *J. Clean. Prod.* **2022**, *337*, 130467. [CrossRef]
30. Ma, H.-C.; Geng, Y.; Bin, R.-L.; Li, G.-D.; Wang, Y.-Y. Effects of mineral admixtures on time-dependent behavior of high-strength self-compacting concrete-filled steel tubes. *Eng. Struct.* **2025**, *335*, 120327. [CrossRef]
31. Mazloom, M.; Ramezanianpour, A.A.; Brooks, J.J. Effect of silica fume on mechanical properties of high-strength concrete. *Cem. Concr. Compos.* **2004**, *26*, 347–357. [CrossRef]
32. Ma, S.; Shao, Y.; Li, S.; Chen, J.; Du, W.; Zhang, Z.; Liu, X. Preparation of low-carbon precast concrete with high-content red mud and steel slag mineral admixtures. *J. Build. Eng.* **2025**, *108*, 112931. [CrossRef]

33. Liu, J.; Xu, L.; Liu, J.; Wang, W.; He, R. Experimental study on manufactured sand concrete containing mineral admixture under freeze-thaw cycles. *Constr. Build. Mater.* **2024**, *453*, 138759. [CrossRef]
34. Chen, P.; Zheng, W.; Wang, Y.; Chang, W. Creep model of high-strength concrete containing supplementary cementitious materials. *Constr. Build. Mater.* **2019**, *202*, 494–506. [CrossRef]
35. Li, T.; Liu, B.; Fan, X.; Yuwen, C.; Hou, K.; Chen, W.; Liu, X.; Guo, S.; Zhang, L. High-value utilization of steel slag and red mud: Recovery of platinum from spent aluminum-based catalyst by pyrometallurgy. *J. Environ. Chem. Eng.* **2025**, *13*, 116748. [CrossRef]
36. Nelson Ponnu Durai, T.; Kandasamy, S.; Rajendran Startha Christabel, A. Enhanced mechanical properties in green concrete through innovative blends of GGBFS, alccofine, and metakaolin. *Hybrid Adv.* **2025**, *11*, 100520. [CrossRef]
37. TC-242-MDC, R.T.C. RILEM draft recommendation: TC-242-MDC multi-decade creep and shrinkage of concrete: Material model and structural analysis*. *Mater. Struct.* **2015**, *48*, 753–770. [CrossRef]
38. Hao, L.; Wang, J.; Sheng, L.; Zhang, Q.; Wei, J.; Zhang, H.; Li, X. Synergistic enhancement of power factor and figure-of-merit in tin sulfide-expanded graphite cementitious composites by silica fume and fly ash. *Mater. Sci. Eng. B* **2025**, *321*, 118567. [CrossRef]
39. Papp, V.; Ardelean, I.; Bulátkó, A.; László, K.; Csík, A.; Janovics, R.; Kéri, M. Effect of metakaolin and fly ash on the early hydration and pore structure of Portland cement. *Cem. Concr. Res.* **2025**, *196*, 107928. [CrossRef]
40. Azizi, M.; Samimi, K. Effect of silica fume on Self-compacting Earth Concrete: Compressive strength, durability and microstructural studies. *Constr. Build. Mater.* **2025**, *472*, 140815. [CrossRef]
41. de Souza, P.H.C.; Engvall, K.; Penha, F.M.; Kantarelis, E.; Nazir, S.M. Sustainable pathway towards red mud valorization through biomass thermochemical conversion and metals recovery. *Bioresour. Technol.* **2025**, *434*, 132847. [CrossRef]
42. Peng, G.-F.; Wang, X.-F.; Ding, H.; Jia, Y.-J. Effect of calcined red mud on the mechanical properties and microstructure of ultra-high performance concrete. *Constr. Build. Mater.* **2025**, *484*, 141891. [CrossRef]
43. Nabavian, S.; Shirvani, M.A.; Gholampour, A. Influences of elevated temperature and re-curing on the compressive performance of lightweight concrete containing metakaolin: Experiments and prediction models. *Constr. Build. Mater.* **2025**, *489*, 142111. [CrossRef]
44. Zhang, Z.H.; Liao, J.L.; Ju, J.T.; Dang, Y.J. Treatment process and utilization technology of steel slag in China and abroad. *J. Iron Steel Res.* **2013**, *25*, 1–4. [CrossRef]
45. Goyal, P.K.; Mudgal, M.; Ghosh, P.K. Assessing the viability of using BOF steel slag treated with tartaric acid as coarse aggregate in concrete. *Constr. Build. Mater.* **2024**, *436*, 136912. [CrossRef]
46. Liu, G.; Zhang, C.; Zhang, S.; Guo, C.; Liu, S.; Li, M.; Wu, Y. Effect and mechanism of calcination on improving the hydration activity of titanium extraction slag. *Constr. Build. Mater.* **2024**, *447*, 138144. [CrossRef]
47. Long, H.; Wu, H.; Zhang, H.; Cheng, Z.; Wang, T.; Ren, X.; Zheng, W.; Wang, Y. Effect of pressed-heat and stuffy slag powder on the properties of epoxy coating. *Chin. J. Eng.* **2024**, *46*, 1403–1410.
48. Yu, Q.; Li, C.; Wang, Z.; Deng, A. Study on preparation and properties of unburned ceramsite with steel slag. *IOP Conf. Ser. Mater. Sci. Eng.* **2019**, *677*, 022067. [CrossRef]
49. Jiao, W.; Sha, A.; Liu, Z.; Jiang, W.; Hu, L.; Li, X. Utilization of steel slags to produce thermal conductive asphalt concretes for snow melting pavements. *J. Clean. Prod.* **2020**, *261*, 121197. [CrossRef]
50. *GB/T 19077-2016*; Particle Size Analysis-Laser Diffraction Methods. Standardization Administration of China: Beijing, China, 2016.
51. Liu, Q.; Liu, J.; Qi, L. Effects of temperature and carbonation curing on the mechanical properties of steel slag-cement binding materials. *Constr. Build. Mater.* **2016**, *124*, 999–1006. [CrossRef]
52. Kumar, S.; Shukla, A.K.; Sharma, A.K.; Kadabinakatti, S. Enhancement of subgrade soil properties using coal bottom ash and basalt fiber for sustainable pavement applications. *Transp. Eng.* **2025**, *21*, 100377. [CrossRef]
53. Li, M.; Bao, S.; Zhang, Y.; Huang, M. Preparation and characterization of low-activity coal bottom ash-based cementitious materials via orthogonal experiment. *J. Build. Eng.* **2024**, *96*, 110495. [CrossRef]
54. Wang, J.; Feng, C.; Wang, Y.; Du, M.; Luo, W.; Zhao, X.; Zhang, W.; Zhu, J. Study on the method of reinforcing recycled fine aggregate by wrapping slag and cement powder. *Constr. Build. Mater.* **2025**, *483*, 141771. [CrossRef]
55. *GB/T1346-2011*; Test Methods for Water Requirement of Normal Consistency, Setting Time and Soundness of the Portland Cement. Standardization Administration of China: Beijing, China, 2011.
56. *GB/T 17671-1999*; Method of Testing Cements-Determination of Strength. Standardization Administration of China: Beijing, China, 1999.
57. *GB5749-2022*; Standards for Drinking Water Quality. Standardization Administration of China: Beijing, China, 2022.
58. *GB 8978-1996*; Integrated Wastewater Discharge Standard. Standardization Administration of China: Beijing, China, 1996.

Disclaimer/Publisher's Note: The statements, opinions and data contained in all publications are solely those of the individual author(s) and contributor(s) and not of MDPI and/or the editor(s). MDPI and/or the editor(s) disclaim responsibility for any injury to people or property resulting from any ideas, methods, instructions or products referred to in the content.